

Track Structures and Dose Distributions from Decays of ^{131}I and ^{125}I in and around Water Spheres Simulating Micrometastases of Differentiated Thyroid Cancer

Wei Bo Li,¹ Werner Friedland, Ekkehard Pomplun,² Peter Jacob, Herwig G. Paretzke, Michael Lassmann³ and Christoph Reiners³

GSF-National Research Center for Environment and Health, Institute of Radiation Protection, 85764 Neuherberg, Germany

Li, W. B., Friedland, W., Pomplun, E., Jacob, P., Paretzke, H. G., Lassmann, M. and Reiners, C. Track Structures and Dose Distributions from Decays of ^{131}I and ^{125}I in and around Water Spheres Simulating Micrometastases of Differentiated Thyroid Cancer. *Radiat. Res.* 156, 419–429 (2001).

The disintegration of the radionuclides ^{131}I and ^{125}I and the subsequent charged-particle tracks left behind in water (as a model substance for a biological cell) are simulated by the Monte Carlo track structure simulation code PARTRAC, using new inelastic electron scattering cross sections for condensed water. Every photon and electron emitted was followed in detail, event by event, down to 10 eV. From the spatial information on the track structures, absorbed dose distributions per ^{131}I and ^{125}I decay were calculated in and around water spheres simulating micrometastases as well as in the tissue surrounding such metastases. These radionuclides were assumed to be distributed uniformly inside spheres of different diameters (0.01, 0.03, 0.1, 0.3, 1.0 and 3.0 mm). The respective electron degradation spectra, the nearest-neighbor distance distributions between inelastic events, and the distance distributions for all activations for both iodine radionuclides were calculated. The absorbed fractions of the initial electron energies, absorbed doses and energy depositions, and single-event distributions, $F_1(\epsilon)$, inside the six water spheres described above and in the surrounding tissue were also calculated. The absorbed doses per decay inside the six water spheres, i.e., the calculated S values (listed from 0.01 to 3.0 mm), were 6.8×10^{-4} , 7.2×10^{-5} , 5.5×10^{-6} , 4.9×10^{-7} , 3.1×10^{-8} and 1.8×10^{-9} Gy Bq⁻¹ s⁻¹ for ^{131}I , and 3.4×10^{-3} , 1.7×10^{-4} , 5.1×10^{-6} , 2.0×10^{-7} , 5.6×10^{-9} and 2.2×10^{-10} Gy Bq⁻¹ s⁻¹ for ^{125}I . It is concluded that, in the treatment of thyroid cancer, the geometrical track structure properties of ^{125}I might be superior to those of ^{131}I in micrometastases with diameters less than 0.1 mm; however, in this medical context, many other factors also have to be considered. © 2001 by Radiation Research Society

INTRODUCTION

Micrometastases of differentiated thyroid cancer are a relatively typical feature of childhood thyroid cancer (1–4). This can be seen in the data from our ongoing treatment of children from Belarus with radiation-induced thyroid cancer (5). The histology shows that most of the children suffered from the papillary version of differentiated thyroid cancer (5); 50% of the children treated in Würzburg had micrometastases in the lung which were not visible on planar radiographs but were visible in post-treatment scans with radioiodine. This means that the metastases of these patients—located mainly in the lungs—had diameters of less than 3–4 mm. Complete remission was achieved in only 43 of 74 children (58%). Therefore, it is questionable whether ^{131}I is the radionuclide of choice for the treatment of such small lung metastases of differentiated thyroid cancer, as has been pointed out by Sisson *et al.* (6) and Maxon *et al.* (7). In particular, the paper by Maxon *et al.* (7) stimulated us to apply the most recent version of the charged-particle track structure code PARTRAC to the calculation of dose distributions from ^{125}I and ^{131}I in and around water spheres simulating micrometastases of diameters between 10 μm and 3 mm. These geometries cover the range of sizes of the lung metastases observed.

The results can be applied particularly to the metastases of papillary thyroid cancer, since there is no evidence that these small metastases show a colloidal structure. They can also be applied to the dosimetry of certain other solid tumors. Recently, several authors discussed the efficacy of radioimmunotherapy for *in vitro* studies using either high-energy β -particle emitters, such as ^{131}I or ^{90}Y , or Auger electron-emitting radionuclides (8–10). Our calculated dosimetry for spheres with sizes covering several orders of magnitude may improve the understanding of their findings.

MATERIALS AND METHODS

Decays of ^{131}I and ^{125}I

The isotope ^{131}I decays by means of six β -particle transitions (11). The total β -particle spectrum of ^{131}I is calculated by summing the six inde-

¹ Author to whom correspondence should be addressed at GSF-National Research Center for Environment and Health, Institute of Radiation Protection, 85764 Neuherberg, Germany; e-mail: wli@gsf.de.

² Current address: Department of Safety and Radiation Protection, Research Center Jülich, 52425 Jülich, Germany.

³ Current address: Clinic for Nuclear Medicine, University of Würzburg, 97080 Würzburg, Germany.

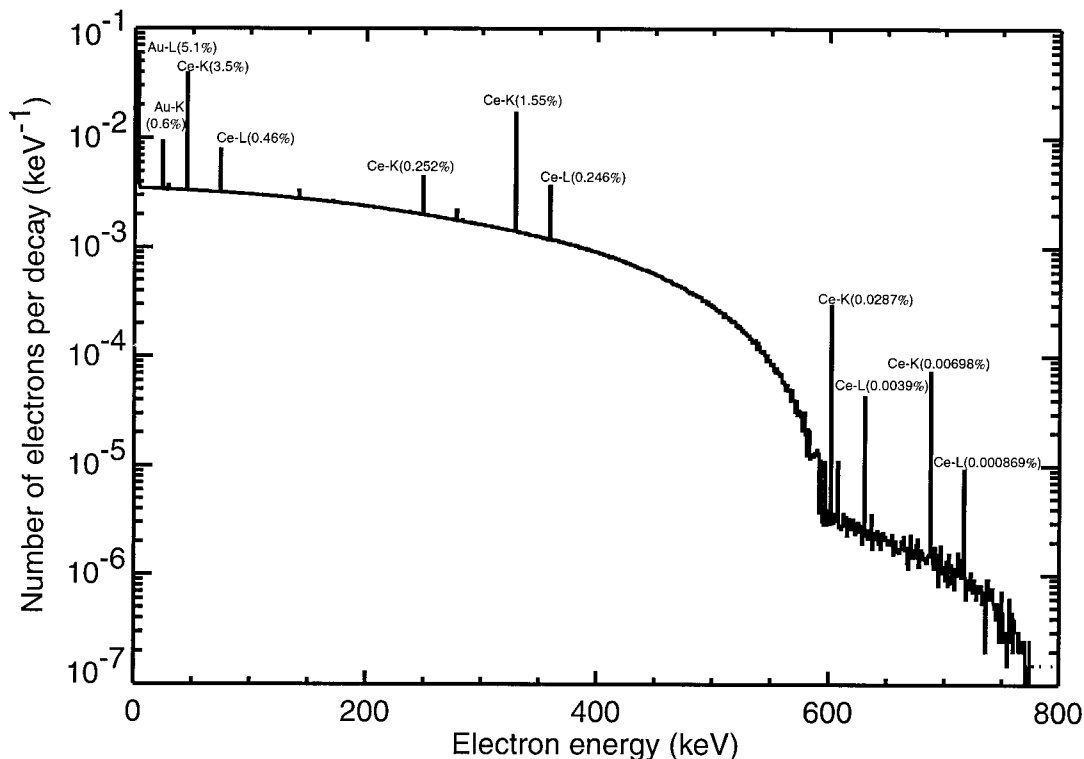


FIG. 1. The primary electron spectra of ^{131}I decay.

pendent transition spectra (12–14), weighted according to their yields. First forbidden nonunique transitions have allowed shapes (12, 13). Therefore, there is only one decay mode (β^-) which was corrected with a shape factor $a_n(W,Z)$. For a first forbidden unique transition, the shape factor of Konopinsky and Rose (15) was used in this calculation; the form of the shape factor was based on Evans (16) and Wu (17). After each β -particle decay, γ rays are emitted, competing with electron ejection by internal conversion. The conversion electron leaves a vacancy in the atom that is filled by electrons from outer shells with emission of characteristic X rays or Auger electrons. In simulating the decay of ^{131}I , all of the possible de-excitation pathways are taken into account with a Monte Carlo method. The energies of the γ rays emitted from the daughter

atom ^{131}Xe are obtained from the difference between the final and initial energies given in refs. (18, 19). The calculated β -particle spectrum of ^{131}I decay agrees well with the summary data from ORNL (12, 13, 20). Figure 1 indicates the mean primary electron spectrum of ^{131}I decays, including internal conversion and Auger electrons, as well as the electron emitted in tissues by the interactions of photons, as simulated by the PARTRAC code (21–23) used in this study.

The spectra of Auger electrons and photons for individual ^{125}I decays have been simulated by the Monte Carlo method described in detail by Pomplun *et al.* (24); references for the probability data used for electron capture, internal conversion, and radiative and radiationless transitions are also given there. The primary electron hole leading to an excited state of the nuclide is created by electron capture mainly from the K shell. For de-excitation by both radiative and Auger processes, Coster-Kronig transitions and shakeoff and double Auger processes are considered. Other processes are neglected here, due either to very low intensities or to a lack of data. Figure 2 gives the resulting distribution of electron (summed) energy released in a single decay. For previous Monte Carlo simulations of ^{125}I decays, see refs. (25, 26).

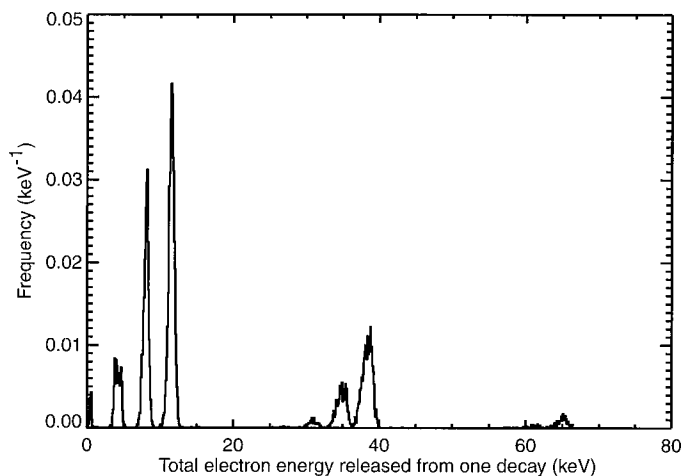


FIG. 2. The frequency of the total electron energy released from one ^{125}I decay.

Track Structure Calculations

The PARTRAC code is a Monte Carlo program that can simulate complete histories of photon and electron interactions from their respective starting energies down to 10 eV (21–23) and can calculate the spatial coordinates of primary activations and chemical modifications in the target material. A source term module describing the photons and electrons emitted in each stochastic decay of ^{131}I and ^{125}I was developed as described above and integrated into PARTRAC. For the transport of photons, three types of inelastic interactions (photoelectric absorption, incoherent Compton scattering, and pair production) and elastic interaction [i.e. coherent (Rayleigh) scattering] are taken into account. The history number, energy, event position in time and space, type of event, track segment length, and direction cosines of all outgoing photons and elec-

trons are recorded. Electrons are followed event by event through their interaction histories in liquid water using the newly derived inelastic cross-section data for liquid water (27). Decays of ¹³¹I and ¹²⁵I were each simulated with lower cutoff energies of 10 eV for electrons and 100 eV for photons; below these values, the residual energy was assumed to be absorbed locally.

The patterns of biological effects and their induction probabilities after the interaction of ionizing radiation with cells and tissues depend on the details of the time and space coordinates of the events in the particle tracks after each interaction. They are the cause of the changes observed later, such as, e.g., dose-effect relationships, dose-rate effects, and radiation quality and effects (23). As mentioned above, the two iodine isotopes considered here have quite different nuclear decay characteristics, which lead to quite different track structures in the surrounding cells and tissues, even at the same absorbed dose. This will be considered in detail in another publication. In this paper, we compare only two basic quantities, the degradation spectra and the neighborhood distributions (23). The degradation spectrum, $Y(E)$, gives the differential path lengths per energy interval from one decay and for all secondary electrons during complete slowing down as a function of the actual energy E . We write $Y(E) = [N(E)]/(dE/dx)$, where $N(E)$ is the absolute number of all secondary and higher-order electrons created by complete slowing down of one decay, which have an initial kinetic energy larger than E . The k -nearest-neighbor (k -NN) rule is one simple nonparametric decision procedure in pattern classification (28). For $k = 1$, this represents the frequency of the distances by taking every inelastic activation (including ionization and excitation) to its nearest neighbor in each track induced by one decay. For increasing k , depending on the cut distance one calculates, this distribution indicates the frequency of the distances by taking every primary activation to all others in every track from one decay (23).

Microdosimetric Single-Event Distribution

The single-event energy deposition, $f_1(\varepsilon)$, is obtained by recording the energy imparted in the volume of interest for each single energy deposition event. The single-event probability in specific energy, $f_1(z)$, which is used more often in microdosimetry, is obtained by recording the imparted energy per unit mass in the volume of interest. $F_1(z)$, defined as $F_1(z) = \int_0^z f_1(z') dz'$, is the conditional probability that a specific energy less than or equal to z is deposited by a single energy deposition event (29, 30), where $z = \varepsilon/m = (1/m) \sum_i \varepsilon_i$, ε is the energy imparted to the matter in a volume with mass m , and ε_i is the energy deposited in a single interaction, i . In our simulations, one disintegration of a radioiodine atom includes one or more photons and electrons. The tracks produced by these primary electrons and their secondary or higher-order δ rays, statistically correlated with all the electrons that were ejected by these primary photons, are regarded as one energy deposition event. These distributions were calculated to provide input for radiobiological models of the action of radiation based on microdosimetric concepts (31).

Geometry and Dose Distribution

Metastases are modeled as spheroids with diameters of 0.01, 0.03, 0.1, 0.3, 1.0 and 3.0 mm. The radionuclides of ¹³¹I and ¹²⁵I are assumed to be distributed uniformly inside the spheres. The tissue around the spheres is modeled as a spherical annulus with a thickness of 40 mm. The metastasis-simulating spheres have a uniform density of 1.060 g cm⁻³. Scoring of the track events was performed in concentric spherical shells in equidistant intervals of 10 μ m. Dose distributions as a function of distance from the centers of the spheres are calculated for each of the six geometries. To obtain the dose distribution, 50,000 decays from ¹³¹I and 100,000 decays from ¹²⁵I are simulated, owing to the larger variability of energy deposition in the immediate neighborhood of a decaying nucleus of ¹²⁵I.

RESULTS

Particle Tracks

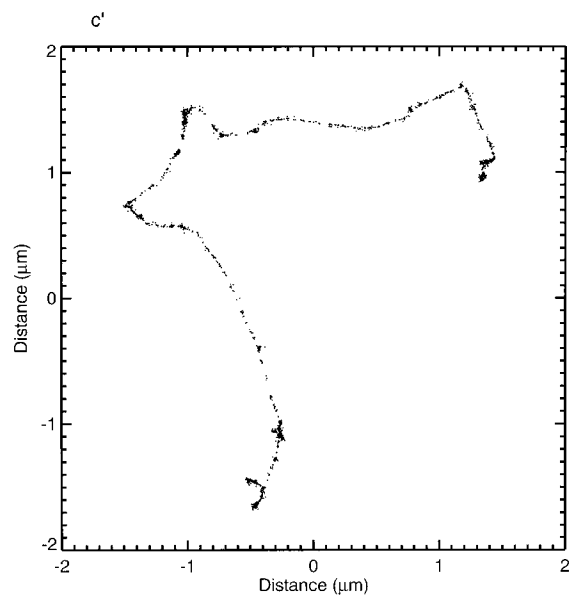
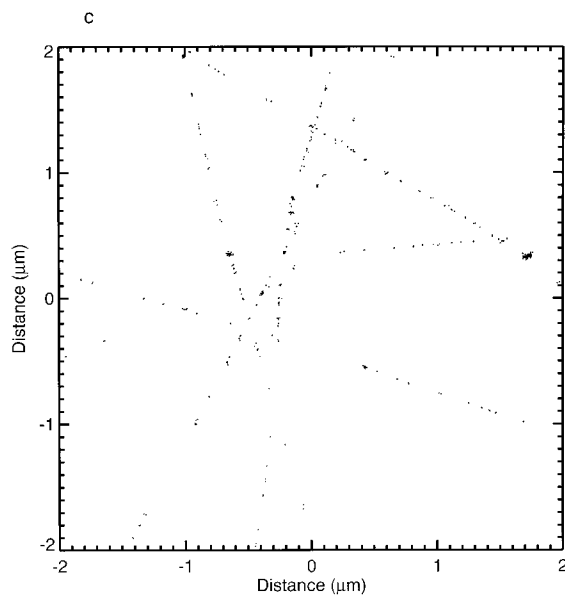
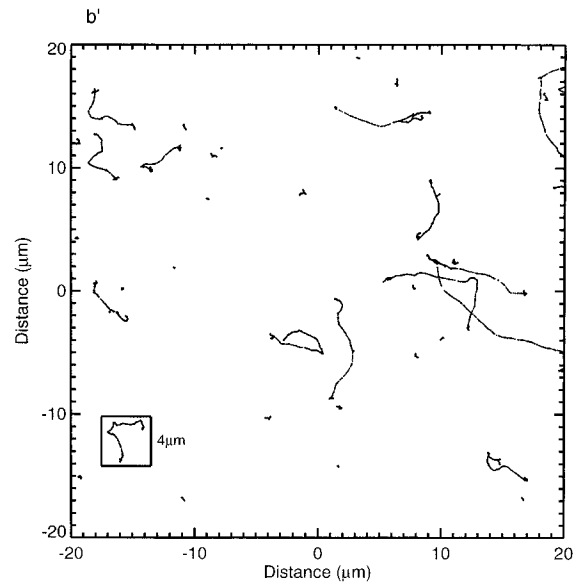
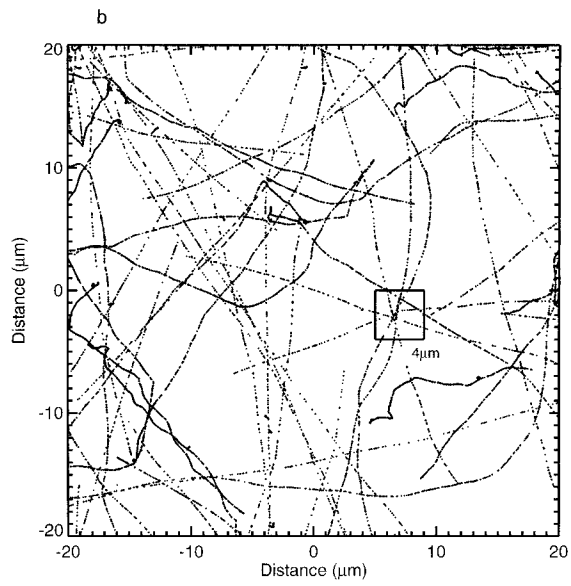
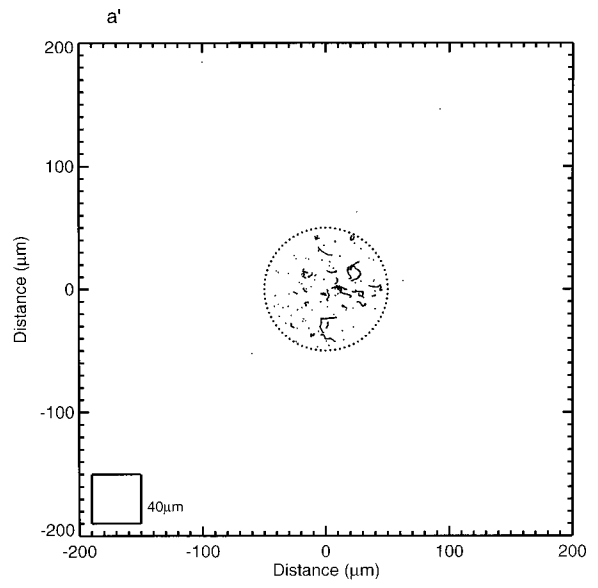
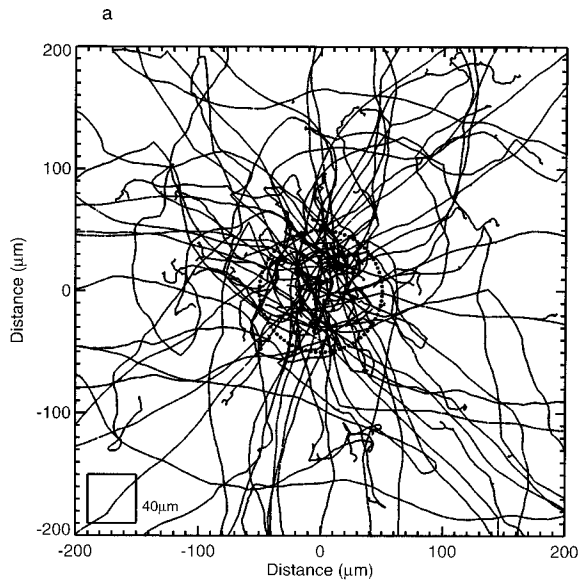
The track structures simulated with the PARTRAC code contain information on every interaction produced by photons and electrons emitted from ¹³¹I and ¹²⁵I decays. Figure 3 shows how the tracks of the decays are structured relative to a "metastasis" 0.1 mm in diameter and in the surrounding tissue in different dimensions. The dominant photon energies of ¹³¹I and ¹²⁵I decays are 364.5 and 27.4 keV, respectively (11), and the mean free paths for 300 and 30 keV photons in tissue are about 10 and 3 cm (23); thus the tracks produced by interactions of photons are far off the scale of this figure. Figure 3a and a' shows that the electron tracks of ¹²⁵I are essentially confined to the "metastasis", due to the range of less than 20 μ m of the dominant conversion electron, with an energy of 3.64 keV, and the principal Auger electrons, with energies of 0.38, 3.02, 3.66 and 22.48 keV. On a smaller scale in Fig. 3b and b', the ranges of the electron tracks from ¹²⁵I are shown to be a few micrometers or less in most cases. Figure 3c and c' presents such tracks in a square of $4 \times 4 \mu\text{m}^2$, showing that the energy deposition in ¹²⁵I tracks is more dense than that in ¹³¹I tracks, again because of the lower kinetic energies of the electrons from ¹²⁵I.

In the lower energy range, ≤ 1 keV, there is no difference in the relative shape of the respective degradation spectra of the electron tracks produced by decays of the two iodine nuclides, except for a factor of about 10 (Fig. 4) due to the accumulation of secondary and higher-order electrons from primary electrons and photoelectrons. With increasing energy, however, ¹²⁵I has relatively more electrons around an energy of 10 to 20 keV, whereas ¹³¹I has far more higher-energy electrons (>30 keV).

The nearest-neighbor distributions show that the most frequently occurring nearest-neighbor distance is about 0.4 nm for both iodine isotopes. The most frequently occurring distances between all activations are 2.6 nm for ¹²⁵I and 2.3 nm for ¹³¹I (Fig. 5a and b). It is very clear that the density of ionizations and excitations in tracks of ¹²⁵I is larger than that of ¹³¹I inside a 100- μ m-diameter sphere (Fig. 5a). These distance distributions of nearest neighbors and between all activations inside 40-cm-diameter tissue spheres (Fig. 5b) are reversed, because more activations are produced by the electrons and photoelectrons with larger kinetic energies emitted from an ¹³¹I decay.

Dose Distributions

The absorbed dose per decay in concentric spherical shells around the center of "metastases" of various diameters that contain homogeneously deposited radionuclides is calculated by summing the energy deposited in each shell and dividing by the mass of the corresponding shell. For all sizes of spheres considered and for both radionuclides, the dose distribution within the spheres is characterized by



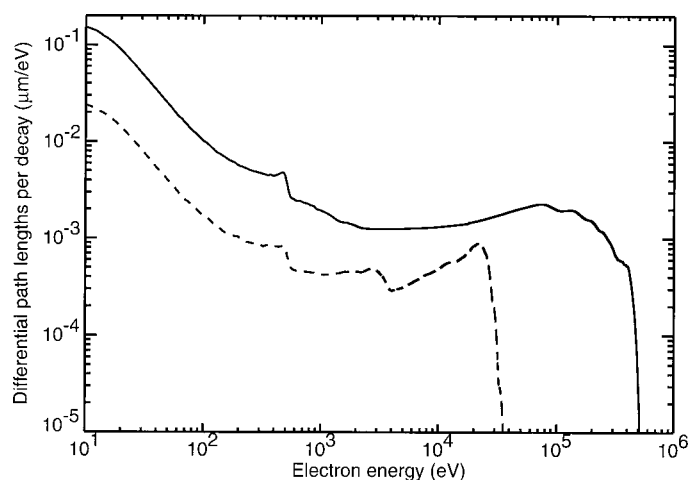


FIG. 4. Degradation spectra per decay of ^{131}I (—) and ^{125}I (---).

a constant value up to its boundary (Fig. 6). In the surrounding tissue at the edge of the spherical “metastases”, the steep slopes of the dose–response curves indicate the very short ranges of the electrons produced inside the “metastases”. The dose per decay also decreases with the increasing radius of the “metastasis” (because of the increasing mass). Comparing spheres of diameters of 0.01 mm and 3 mm, the dose per decay decreases by about a factor of 3×10^5 for ^{131}I and by a factor of 10^7 for ^{125}I . For ^{131}I , the decrease in dose is much less than the inverse of the increase in mass, because an increasing amount of the radiation is absorbed within the “metastasis”. For a 0.1-mm-diameter “metastasis”, the doses per decay of ^{131}I and ^{125}I are approximately equal: At this radius, the high-energy electrons from one ^{131}I decay deposit the same amount of energy on average as that released per ^{125}I decay by electron emission. Corresponding to the short range of primary electrons from ^{125}I , outside of the “metastasis”, the dose decreases sharply over a range of only 0.02 mm; this decrease amounts to a factor of 3×10^4 for a sphere 0.01 mm in diameter and 30 for a sphere 3 mm in diameter. Due to the higher energy of the primary electrons produced by ^{131}I , the decrease in the dose outside the sphere has a smaller slope and extends to a distance of about 1.5 mm from the surface of the sphere; for the smallest “metastasis” (diameter 0.01 mm), the dose decreases by a factor of 3×10^8 over this range and for the largest one (3 mm), by a factor of 300. At a distance of 3 mm from the center of the sphere, the dose per decay is 2×10^{-12} Gy in all cases considered. In the range of 3–20 mm from the center of the sphere, the dose decreases for ^{131}I with a slope of about $d^{-1.5}$.

Single-Event Distribution

The probability distribution $F_1(\varepsilon)$, giving the conditional probability of the imparted energy ε in a volume less than or equal to ε , is shown for the two radionuclides in Fig. 7. There is little evident dependence on sphere radius to be seen for ^{125}I , with its short-range electrons, in contrast to the large influence seen for ^{131}I , with its energetic β particles.

Absorbed Fraction and Energy Deposition around Sphere

From the dose distributions shown in Fig. 6, the energy deposition and average dose inside the sphere, i.e., S values can be calculated; these are presented in Figs. 8 and 9. The energy deposition inside these spheres (Fig. 8) results mainly from the primary electrons and their secondaries for both ^{131}I and ^{125}I , with only a small contribution from photons. The S values (Fig. 9) for ^{125}I are larger than those for ^{131}I inside spheres smaller than 0.1 mm in diameter but are smaller than those of ^{131}I inside larger spheres. Around a diameter d of 0.1 mm, the average energy deposited by ^{131}I increases approximately linearly with d ; therefore, the S value decreases approximately inversely to the square of d . The average energy deposited by ^{125}I is approximately constant in this region, and so its S value falls with the third power of d .

Figure 10 shows the absorbed fraction of the primary electron energy. For ^{131}I , it is always smaller than 1.0, but for ^{125}I , it becomes slightly larger than 1.0 in the 3.0-mm sphere, because the energies of the secondary electrons produced by primary photons also deposit some energy inside the sphere. The energy deposition in shells outside the source as a function of distance from the surface of the spheres with homogeneous radionuclide deposition inside is presented graphically in Fig. 11.

DISCUSSION

Dosimetry calculations for internally distributed radionuclides are often based upon the so-called MIRD schema (32–34). The mean absorbed dose to the total body and to specific organs for systemically administered radionuclides is usually calculated by an analytical method in which accumulated activity in the actual source region, \bar{A} , is multiplied by the mean absorbed dose to the target region per unit cumulated activity in the source region, S (source region \rightarrow target region) (35). In radioiodine therapy, e.g. when the dimension of the tissue is larger than 5 mm, the accumulated dose can be calculated by the total activity admin-

FIG. 3. The track structures of 100 ^{131}I (panels a–c) and 100 ^{125}I (panels a'–c') decays. The sources are assumed to be distributed uniformly in a sphere 0.1 mm in diameter. Each energy deposition event is indicated by a small dot. The circles drawn with dotted lines in panels a and a' denote the circumference of the metastases. The small square in each panel indicates the scale of the next figure: Panels c and c' magnify the tracks shown in panels b and b'.

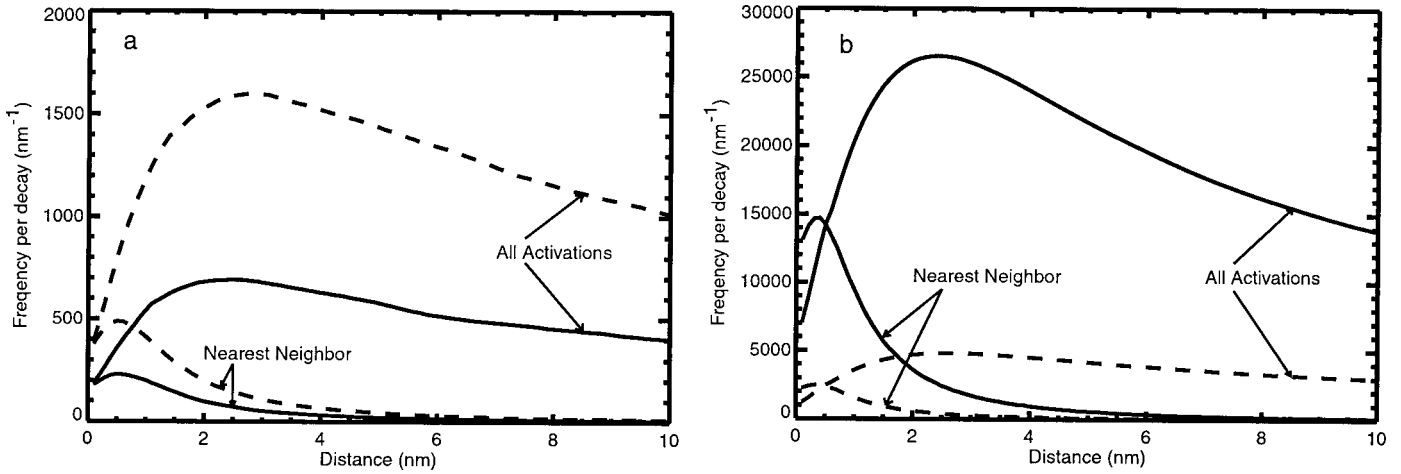


FIG. 5. Nearest-neighbor and all activation distance distributions per decay of ¹³¹I (—) and ¹²⁵I (---). Panel a shows the distributions inside a 100-μm-diameter sphere, and panel b shows the distributions inside a 40-cm-diameter sphere.

istered to the patient, Q , the percentage uptake per gram in tissue, f , and an effective half-time T_e . When the dimension of the tissue is smaller than 5 mm, the dose calculation has to be corrected. The correction depends on the size of the tissue and is given by the fraction of the electron energy absorbed (36), and for β -particle decay, the different components must be added and integrated (37).

S values of ¹³¹I and ¹²⁵I for selected organs have been published previously, e.g. by Snyder *et al.* (33). S values and absorbed doses to small, unit-density spheres with diameters in the millimeter range and above can be obtained,

e.g., from the nodule module of the computer code MIRDOSE 3.1 (38) which implements the data of Snyder *et al.* (33) or from some other newer models for internal dose assessment in nuclear medicine (38). However, the smallest sphere for which the dose can be assessed with this program has a diameter of 2.64 mm. On the small end of the range, at the cellular level, a recent publication by the MIRD committee (39) summarizes S values for selected radionuclides; radiation doses to the cell nuclei in single cells and in cells in clusters after ¹³¹I decay are given, e.g., in ref. (40). Absorbed fractions of ¹³¹I inside large spheres

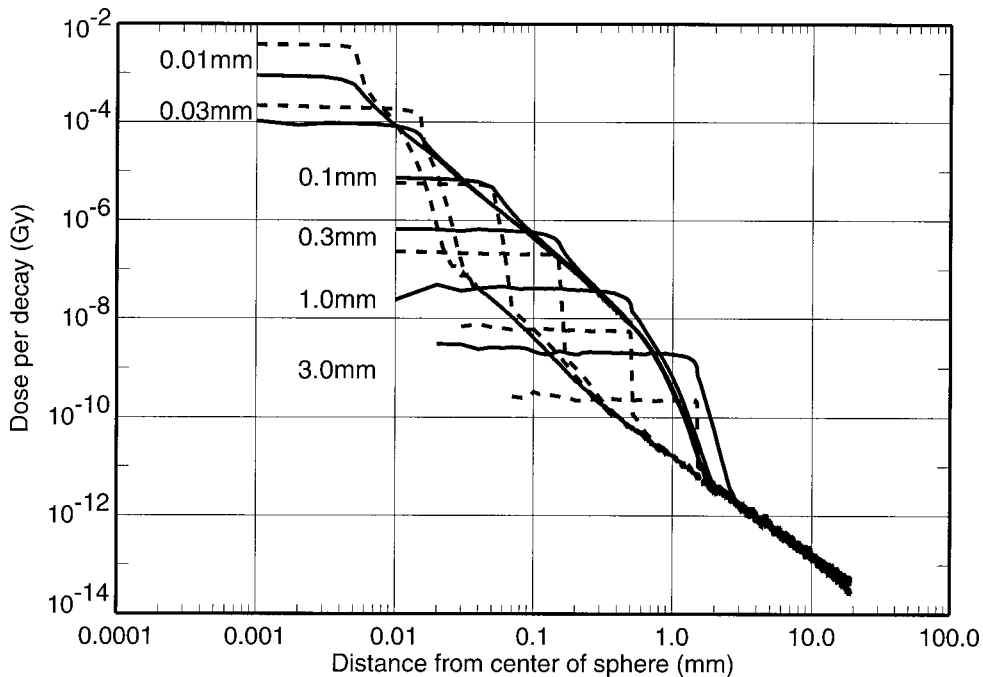


FIG. 6. The dose distribution per ¹³¹I (—) and ¹²⁵I (---) decay in “metastasis” and surrounding tissue. Dose is calculated in a series of concentric shells around each sphere. Dose is calculated for 10-μm-thick shells for the 0.1-, 0.3-, 1.0- and 3.0-mm-diameter spheres and for 1-μm-thick shells for the 0.01- and 0.03-mm-diameter spheres.

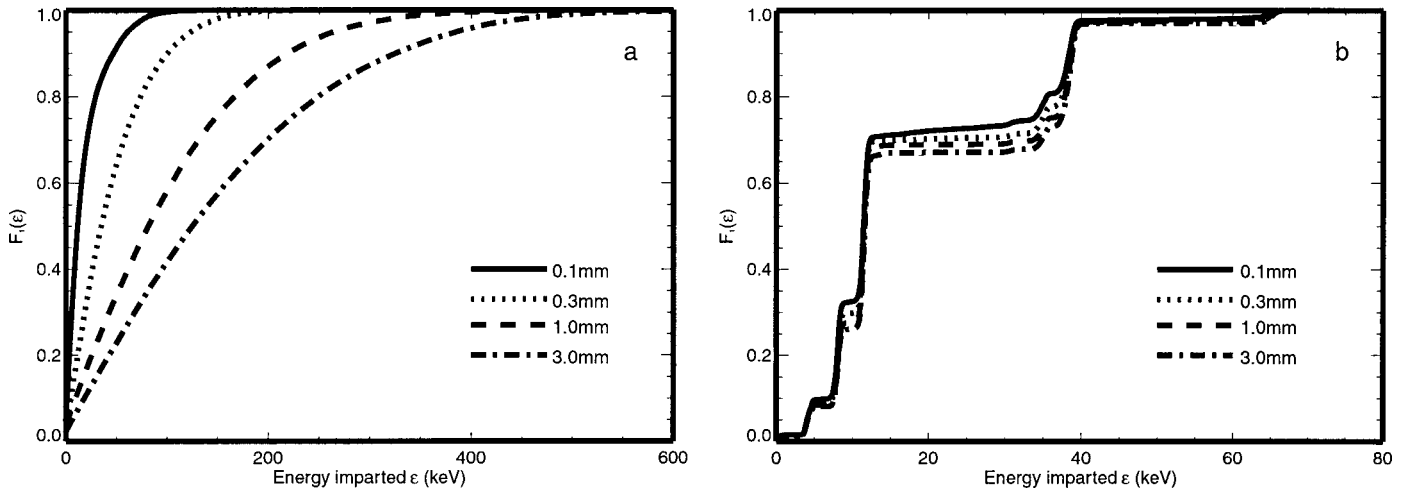


FIG. 7. Single-event distribution, $F_1(\epsilon)$, inside 0.1-, 0.3-, 1.0- and 3.0-mm spheres for ^{131}I (panel a) and ^{125}I (panel b) decays.

1.0, 2.0 and 5.0 cm in diameter, which are beyond the scope of the present work, were calculated by Akabani *et al.* (41) using the spectral method and the average energy method. In Table 1, the analytical MIRD S values from various authors (38, 39, 42) are listed for ^{131}I and ^{125}I in columns 3 and 6 for comparison with present full Monte Carlo results.

The ratios between the S values from our present, very detailed Monte Carlo work and the published values fall into the range of 0.92 to 1.31. For smaller spheres, the S values seem to be underestimated for ^{131}I and overestimated for ^{125}I by using the values published by Goddu *et al.* (42) and MIRD (39), but for ^{131}I in a sphere 0.006 mm in diameter, the S value of MIRD (39) is somewhat larger than

our value. For a larger sphere, the S values given by the computer code of Stabin *et al.* (38) appear to be smaller than ours, particularly for ^{131}I . For spheres with diameters in the millimeter range, this can be explained by the use of only the electron/ β -particle data (38) and by the use of point-source kernels and the results of Berger *et al.* (43) for monoenergetic electrons and β particles. The input data used in those simulations did not include the newest cross sections for photons and electrons (27), which are incorporated in our work.

For small diameters in the micrometer range, a major shortcoming of the results of Goddu *et al.* (42) and of the MIRD values (39) is the use of a stopping-power formalism

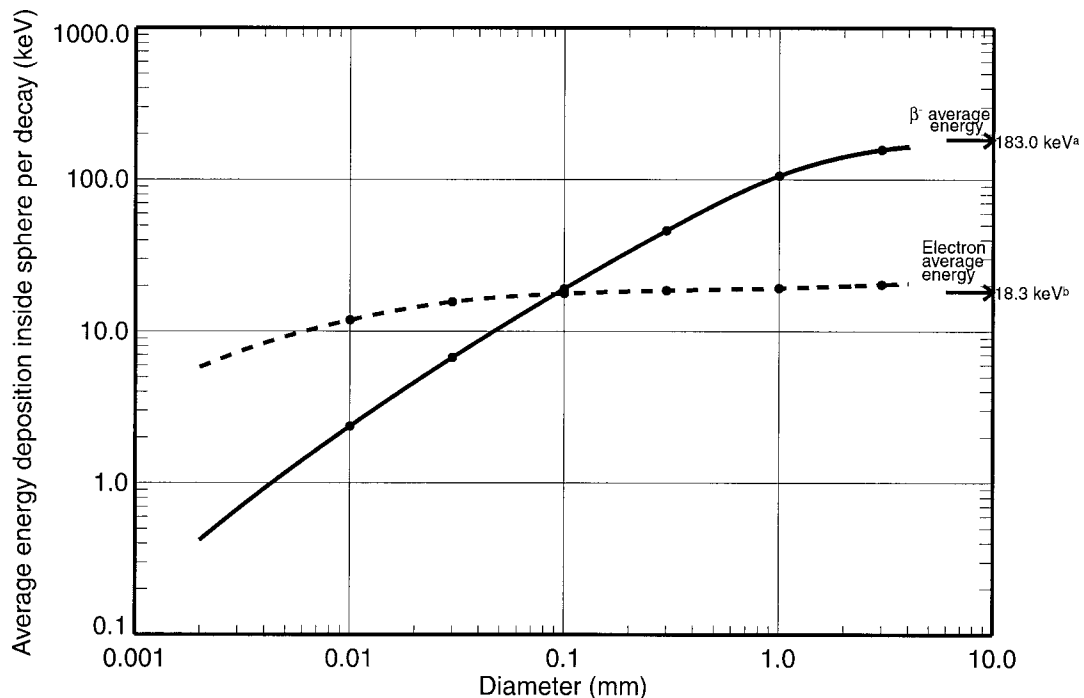


FIG. 8. Energy deposition inside "metastasis". ^aCross *et al.* (12), ^bPomplun *et al.* (24) ^{131}I (—), ^{125}I (---).

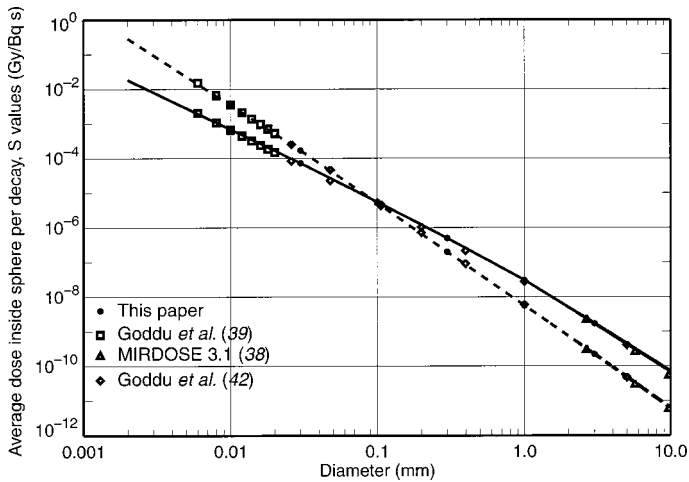


FIG. 9. S values inside “metastasis”. The solid and dashed lines are interpolated by the data for our six simulated diameters ^{131}I (—), ^{125}I (---).

at low energies, which in the cases of ^{125}I and of the low-energy β particles of ^{131}I underestimates the true energy deposition pattern. The shortcomings of the analytical methods applied to the calculation of the cellular S values are discussed extensively by Goddu *et al.* (39). Our calculations are based on Monte Carlo simulations of track structures of ^{131}I and ^{125}I and include the newest data available on the cross sections (27). Therefore, we provide new data on such dose distributions in and around the small spheres. The great advantage of the Monte Carlo track structure simulation is that it is extremely flexible and can be adapted easily to new input data and to any geometry.

There are many other reports of dose calculations in radioiodine therapy, such as those by Sinclair *et al.* (44), Benua *et al.* (35), Beierwaltes (45–47), Saenger *et al.* (48), Schlesinger *et al.* (36), and Maxon *et al.* (7, 49), whose dose estimations are applicable to larger metastases. Jungerman *et al.* (37) and Hartman *et al.* (40) also dealt with ^{131}I and with micrometastases using integration of an analytical point-dose kernel (similar to the MIRD approach). The dose of ^{125}I is often calculated for commercial seed sources (50–53); for such seeds, however, the electrons emitted by ^{125}I decays are completely absorbed by the seed wall and thus do not factor into the tissue dosimetry.

In the case of micronodular lung metastases from papillary thyroid cancer, Sisson *et al.* (6) discuss whether the ^{131}I treatment is ineffective because of the small size of the tumors. Their conclusion is that many lung metastases from papillary thyroid cancer might be too small for effective treatment with ^{131}I , but large doses of ^{131}I may still shrink the tumors. Maxon *et al.* (7) consider the dosimetry of treatment of macrometastases and micrometastases from differentiated thyroid carcinoma with ^{131}I and ^{125}I using S values for tumors with diameters of <0.2 mm (39), $0.1 < d < 2$ mm (unpublished data), and >2.6 mm (38). Their calculations using modified S values reveal that a treatment

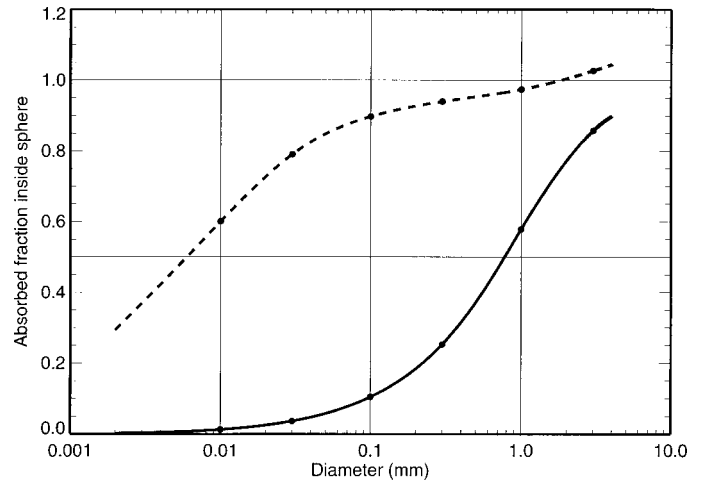


FIG. 10. Absorbed fraction inside spheres. For ^{125}I decay inside spheres more than 3 mm in diameter, the absorbed fraction is slightly larger than 1 due to the electron energy deposition events produced by photons inside these spheres. ^{131}I (—), ^{125}I (---).

with ^{125}I might deliver a higher dose to small metastases than treatment with ^{131}I (7). The authors propose treatment with ^{125}I or with a mixture of $^{125}\text{I}/^{131}\text{I}$, which seems to be more effective in the case of pulmonary metastases of thyroid cancer.

The retention and toxicities of the longer-lived ^{125}I decay in bone marrow and other normal tissues, however, must also be taken into account when treatment with a mixture of ^{125}I and ^{131}I is applied. One must also keep in mind that a single thyroid cancer cell will receive only a transient exposure to iodine, whereas a larger micrometastasis could store the iodine for several days. In addition, the uniform distribution of ^{125}I in the spherical metastases assumed in our simulation could overestimate the real dose to target nuclei, since most of the ^{125}I in tumors is in the colloid and is not distributed uniformly (7). For small metastases of

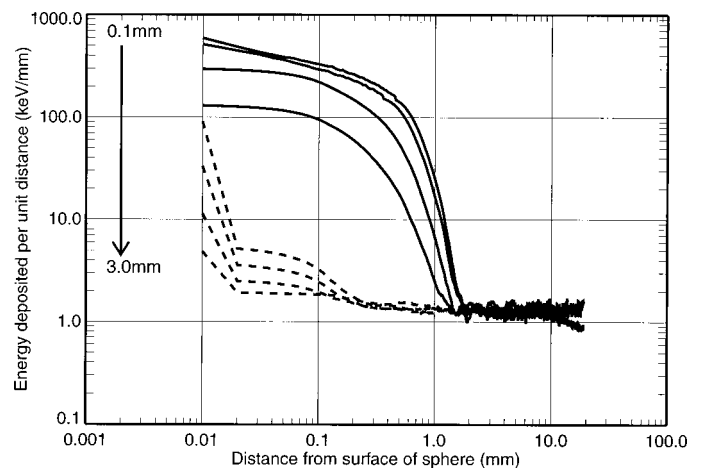


FIG. 11. Energy deposition per unit distance per decay in each 10- μm concentric spherical shell around the surface of the sphere. ^{131}I (—), ^{125}I (---).

TABLE 1
Comparison of the S Values in the Present Work and in the MIRD Committee Calculations

Diameter (mm)	¹³¹ I			¹²⁵ I		
	Present work (Gy/Bq s)	MIRD ^c (Gy/Bq s)	Ratio PW ^e /MIRD	Present work (Gy/Bq s)	MIRD ^c (Gy/Bq s)	Ratio PW ^e /MIRD
0.006	1.94×10^{-3a}	2.02×10^{-3}	0.96	1.40×10^{-2a}	1.52×10^{-2}	0.92
0.008	1.07×10^{-3a}	1.07×10^{-3}	1.00	6.33×10^{-3a}	6.67×10^{-3}	0.95
0.010	6.80×10^{-4}	6.57×10^{-4}	1.04	3.40×10^{-3}	3.54×10^{-3}	0.96
0.012	4.69×10^{-4a}	4.43×10^{-4}	1.06	2.08×10^{-3a}	2.12×10^{-3}	0.98
0.014	3.42×10^{-4a}	3.18×10^{-4}	1.07	1.36×10^{-3a}	1.38×10^{-3}	0.99
0.016	2.60×10^{-4a}	2.39×10^{-4}	1.09	9.42×10^{-4a}	9.58×10^{-4}	0.98
0.018	2.04×10^{-4a}	1.85×10^{-4}	1.10	6.82×10^{-4a}	6.94×10^{-4}	0.98
0.020	1.65×10^{-4a}	1.48×10^{-4}	1.11	5.10×10^{-4a}	5.20×10^{-4}	0.98
0.026	9.62×10^{-5}	8.37×10^{-5d}	1.15	2.48×10^{-4}	2.53×10^{-4d}	0.98
0.030	7.20×10^{-5}			1.70×10^{-4}		
0.048	2.64×10^{-5}	2.25×10^{-5d}	1.17	4.29×10^{-5}	4.59×10^{-5d}	0.93
0.100	5.50×10^{-6}			5.10×10^{-6}		
0.106	4.85×10^{-6}	4.20×10^{-6d}	1.15	4.32×10^{-6}	4.66×10^{-6d}	0.93
0.20	1.20×10^{-6}	1.03×10^{-6d}	1.16	6.60×10^{-7}	7.17×10^{-7d}	0.93
0.30	4.90×10^{-7}			2.00×10^{-7}		
0.40	2.54×10^{-7}	2.16×10^{-7d}	1.18	8.46×10^{-8}	9.13×10^{-8d}	0.93
1.00	3.05×10^{-8}	2.80×10^{-8d}	1.09	5.56×10^{-9}	5.91×10^{-9d}	0.94
2.64	2.35×10^{-9a}	2.34×10^{-9b}	1.00	3.17×10^{-10a}	3.11×10^{-10b}	1.02
3.0	1.80×10^{-9}			2.20×10^{-10}		
5.0	4.35×10^{-10}	4.01×10^{-10d}	1.08	4.81×10^{-11}	4.75×10^{-11d}	1.01
5.69	3.09×10^{-10a}	2.70×10^{-10b}	1.14	3.28×10^{-11a}	3.11×10^{-11b}	1.05
9.73	7.49×10^{-11a}	5.70×10^{-11b}	1.31	6.74×10^{-12a}	6.22×10^{-12b}	1.08

^a Data interpolated from our calculated diameters.

^b Data calculated by the computer code MIRDOSE 3.1 (38).

^c Data taken from Goddu *et al.* (39).

^d Data taken from Goddu *et al.* (42).

^e Present work.

papillary thyroid cancer, this is not a problem, since there is no evidence that metastases of papillary thyroid cancer show a colloidal structure. If there are better data available on the microscopic structure of small metastases of differentiated thyroid cancer, our track structure calculation method has the advantage of being capable of modeling any realistic distribution of ¹²⁵I atoms in small colloid tumors.

Another advantage of applying Auger-electron emitters such as ¹²⁵I for the treatment of metastases of differentiated thyroid cancer and/or solid tumors is the fact that the non-specific toxicity to other cells and/or the dose to the bone marrow due to the circulation of the radionuclide in blood might be greatly reduced (10).

The results of this present work on the physical characteristics of microscopic energy deposition around the two radioisotopes of iodine represent only one of many factors that must be assessed when considering using ¹²⁵I for therapy. In addition, the biological behavior, retention and toxicity of iodine in normal and tumor tissues must be taken into account.

ACKNOWLEDGMENT

This work was supported by the EC under contract No. EC-FI4C-CT96-0009.

Received: June 13, 2000; accepted: June 26, 2001

REFERENCES

1. M. Schlumberger, F. De Vathaire, J. P. Travagli, G. Vassal, J. Lemerle, C. Parmentier and M. Tubiana, Differentiated thyroid carcinoma in childhood: Long term follow-up of 72 patients. *J. Clin. Endocrinol. Metab.* **65**, 1088–1094 (1987).
2. R. Vassilopoulou-Sellin, M. J. Klein, T. H. Smith, N. A. Samaan, R. A. Frankenthaler, H. Goepfert, A. Cangir and T. P. Haynie, Pulmonary metastases in children and young adults with differentiated thyroid cancer. *Cancer* **71**, 1348–1352 (1993).
3. C. Reiners, J. Biko, N. Kruglova and E. P. Demidchik, Therapy of thyroid carcinoma in children from Belarus after the Chernobyl accident. In *The Thyroid and Iodine* (J. Nauman, D. Glinoe, L. E. Braverman and U. Hostalek, Eds.), pp. 89–97. Schattauer, Stuttgart and New York, 1996.
4. M. E. Dottorini, A. Vignati, L. Mazzucchelli, G. Lomuscio and L. Colombo, Differentiated thyroid carcinoma in children and adolescents: A 37-year experience in 85 patients. *J. Nucl. Med.* **38**, 669–675 (1997).
5. C. Reiners, J. Biko, J. Farahati, S. Danilovna, V. Drozd and E. P. Demidchik, Results of radioiodine treatment in 158 children from Belarus with thyroid cancer after the Chernobyl accident. In *Radiation and Thyroid Cancer* (G. Thomas, A. Karaoglou and E. D. Williams, Eds.), pp. 407–410. World Scientific, Singapore, 1999.
6. J. Sisson, D. Jamadar, E. Kazerooni, T. Giordano and S. Spaulding, I-131 treatment of micronodular lung metastases from papillary thyroid cancer: Are the tumors too small? *Thyroid* **7**, 312 (1997).
7. H. R. Maxon, S. R. Thomas and R. C. Samaratinga, Dosimetric considerations in the radioiodine treatment of macrometastases and

- micrometastases from differentiated thyroid cancer. *Thyroid* **7**, 183–187 (1997).
8. T. M. Behr, G. Sgouros, V. Vougiokas, S. Memtsoudis, S. Gratz, H. Schmidberger, R. D. Blumenthal, D. M. Goldenberg and W. Becker, Therapeutic efficacy and dose-limiting toxicity of Auger-electron vs. beta emitters in radioimmunotherapy with internalizing antibodies: Evaluation of ¹²⁵I- vs. ¹³¹I-labeled CO17-1A in a human colorectal cancer model. *Int. J. Cancer* **76**, 738–748 (1998).
 9. T. M. Behr, M. Behe, M. Lohr, G. Sgouros, C. Angerstein, E. Wehrmann, K. Nebendahl and W. Becker, Therapeutic advantages of Auger electron- over beta-emitting radiometals or radioiodine when conjugated to internalizing antibodies. *Eur. J. Nucl. Med.* **27**, 753–765 (2000).
 10. S. V. Govindan, D. M. Goldenberg, S. E. Elsamra, G. L. Griffiths, G. L. Ong, M. W. Brechbiel, J. Burton, G. Sgouros and M. J. Mattes, Radionuclides linked to a CD74 antibody as therapeutic agents for B-cell lymphoma: Comparison of Auger electron emitters with beta-particle emitters. *J. Nucl. Med.* **41**, 2089–2097 (2000).
 11. ICRP, *Radionuclide Transformations: Energy and Intensity of Emission*. Publication 38, International Commission on Radiological Protection, Pergamon Press, Oxford, 1983.
 12. W. C. Cross, H. Ing and N. Freedman, A short atlas of beta-ray spectra. *Phys. Med. Biol.* **28**, 1251–1260 (1983).
 13. ICRU, *Dosimetry of External Beta Rays for Radiation Protection*. Report No. 56, International Commission on Radiation Units and Measurements, Bethesda, MD, 1997.
 14. H. Behrens and J. Jänecke, Numerical tables for beta-decay and electron capture, In *Landolt-Börnstein Numerical Data and Functional Relationships in Science and Technology New series Group I: Nuclear Physics and Technology*, Vol. 4 (H. Schopper and K-H. Hellwege, Eds.). Springer-Verlag, Berlin, Heidelberg and New York, 1969.
 15. E. J. Konopinsky and M. E. Rose, The theory of nuclear β -decay. In *Alpha-, Beta- and Gamma ray Spectroscopy*, Vol. 2 (K. Siegbahn, Ed.), pp. 1327–1364. North-Holland, Amsterdam, 1965.
 16. R. D. Evans, *The Atomic Nucleus*. McGraw-Hill, New York, 1956.
 17. C. S. Wu, O. Kofoed-Hansen, M. Goldhaber, L. Grodzins, A. W. Sunyar, H. Frauenfelder, R. M. Steffen, F. Reines, S. P. Rosen and H. Primakoff, The experimental determination of the beta-interaction. In *Alpha-, Beta- and Gamma ray Spectroscopy*, Vol. 2 (K. Siegbahn, Ed.), pp. 1365–1390. North-Holland, Amsterdam, 1965.
 18. *Nuclear Structure and Decay Data*. National Nuclear Data Center, Brookhaven National Laboratory, Upton, NY, 1998.
 19. J. A. Bearden and A. F. Burr, Reevaluation of X-ray atomic energy level. *Rev. Mod. Phys.* **39**, 125–142 (1967).
 20. M. J. Dillman, *EDISTER—A Computer Program to Obtain a Nuclear Decay Data Base for Radiation Dosimetry*. Report ORNL TM-6689, Oak Ridge National Laboratory, Oak Ridge, TN, 1980.
 21. W. Friedland, P. Jacob, H. G. Paretzke and T. Stork, Monte Carlo simulation of the production of short fragments by low-linear energy transfer radiation using higher-order DNA models. *Radiat. Res.* **150**, 170–182 (1998).
 22. S. Henß and H. G. Paretzke, Biophysical modeling of radiation induced damage in chromosome. In *Biophysical Modeling of Radiation Effects* (K. H. Chadwick, G. Moschini and N. M. Varma, Eds.), pp. 67–76. Adam Hilger, Bristol, 1992.
 23. H. G. Paretzke, Radiation track structure theory. In *Kinetics of Non-homogeneous Processes* (G. R. Freeman, Ed.), pp. 89–170. Wiley, New York, 1987.
 24. E. Pomplun, J. Booz and D. E. Charlton, A Monte Carlo simulation of Auger cascades. *Radiat. Res.* **111**, 533–552 (1987).
 25. D. E. Charlton and J. Booz, A Monte Carlo treatment of the decay of ¹²⁵I. *Radiat. Res.* **87**, 10–23 (1981).
 26. J. Booz, H. G. Paretzke, E. Pomplun and P. Olko, Auger-electron cascades, charged potential and microdosimetry of iodine-125. *Radiat. Environ. Biophys.* **26**, 151–162 (1987).
 27. M. Dingfelder, D. Hantke, M. Inokuti and H. G. Paretzke, Electron inelastic-scattering cross sections in liquid water. *Radiat. Chem.* **53**, 1–18 (1998).
 28. T. M. Cover and P. E. Hart, Nearest neighbor pattern classification. *IEEE Trans. Inform. Theory* **11**, 21–27 (1967).
 29. ICRU, *Microdosimetry*. Report No. 36, International Commission on Radiation Units and Measurements, Bethesda, MD, 1983.
 30. ICRU, *Fundamental Quantities and Units for Ionizing Radiation*. Report No. 60, International Commission on Radiation Units and Measurements, Bethesda, MD, 1998.
 31. H. H. Rossi and M. Zaider, *Microdosimetry and Its Application*. Springer-Verlag, Berlin, Heidelberg and New York, 1996.
 32. R. Loevinger and M. Berman, A formalism for calculation of absorbed dose from radionuclides. *Phys. Med. Biol.* **13**, 205–217 (1968).
 33. W. S. Snyder, M. R. Ford and G. G. Warner, *S—Absorbed Dose per Unit Cumulated Activity for Selected Radionuclides and Organs*. MIRD Pamphlet 11, Society of Nuclear Medicine, New York, 1975.
 34. R. Loevinger, T. F. Budinger and E. E. Watson, *MIRD Primer for Absorbed Dose Calculations*. Society of Nuclear Medicine, New York, 1988.
 35. R. S. Benua, N. R. Cicale, M. Sonenberg and R. W. Rawson, The relation of radioiodine dosimetry to results and complications in the treatment of metastatic thyroid cancer. *Am. J. Roentgenol. Radiat. Ther. Nucl. Med.* **87**, 171–182 (1962).
 36. T. Schlesinger, M. A. Flower and V. R. McCready, Radiation dose assessments in radioiodine (¹³¹I) therapy. 1. The necessity for *in vivo* quantitation and dosimetry in the treatment of carcinoma of the thyroid. *Radiother. Oncol.* **14**, 35–41 (1989).
 37. J. A. Jungerman, K. P. Yu and C. I. Zanelli, Radiation absorbed dose estimates at the cellular level for some electron-emitting radionuclides for radioimmunotherapy. *Int. J. Appl. Radiat. Isot.* **35**, 883–888 (1984).
 38. M. G. Stabin, MIRDOSE: Personal computer software for internal dose assessment in nuclear medicine. *J. Nucl. Med.* **37**, 538–546 (1996).
 39. S. M. Goddu, R. W. Howell, L. G. Bouchet, W. E. Bolch and D. V. Rao, *MIRD Cellular S Values*. Society of Nuclear Medicine, Reston, VA, 1997.
 40. T. Hartman, H. Lundqvist, J. Westlin and J. Carlsson, Radiation doses to the cell nucleus in single cells and cells in micrometastases in targeted therapy with ¹³¹I labeled ligands or antibodies. *Int. J. Radiat. Oncol. Biol. Phys.* **46**, 1025–1036 (2000).
 41. G. Akabani, J. W. Poston and W. E. Bolch, Estimates of beta absorbed fractions in small tissue volumes for selected radionuclides. *J. Nucl. Med.* **32**, 835–839 (1991).
 42. S. M. Goddu, D. V. Rao and R. W. Howell, Multicellular dosimetry for micrometastases: Dependence of self-dose versus cross-dose to cell nuclei on type and energy of radiation and subcellular distribution of radionuclides. *J. Nucl. Med.* **35**, 521–530 (1994).
 43. M. J. Berger, *Distribution of Absorbed Doses around Point Sources of Electrons and Beta Particles in Water and other Media*. MIRD Pamphlet No. 7, Society of Nuclear Medicine, New York, 1971.
 44. W. K. Sinclair, J. D. Abbott, H. E. Farran, E. B. Harris and L. F. Lamerton, A quantitative autoradiographic study of radioiodine distribution and dosage in human thyroid glands. *Br. J. Radiol.* **29**, 36–41 (1956).
 45. W. H. Beierwaltes, The history of the use of radioactive iodine. *Semin. Nucl. Med.* **9**, 151–155 (1979).
 46. W. H. Beierwaltes, The treatment of thyroid carcinoma with radioactive iodine. *Semin. Nucl. Med.* **8**, 79–94 (1978).

47. W. H. Beierwaltes, The treatment of hyperthyroidism with iodine-131. *Semin. Nucl. Med.* **8**, 95–103 (1978).
48. E. L. Saenger, J. G. Kereiakes, V. J. Sodd and R. David, Radiotherapeutic agent: Properties, dosimetry, and radiobiologic considerations. *Semin. Nucl. Med.* **9**, 72–84 (1979).
49. H. R. Maxon, E. E. Englaro, S. R. Thomas, V. S. Hertzberg, J. D. Hinnefeld, L. S. Chen, H. Smith, D. Cummings and M. D. Aden, Radioiodine-131 therapy for well-differentiated thyroid cancer—a quantitative radiation dosimetric approach: Outcome and validation in 85 patients. *J. Nucl. Med.* **33**, 1132–1136 (1992).
50. G. S. Burns and D. E. Raeside, Two-dimensional dose distribution around a commercial ^{125}I seed. *Med. Phys.* **15**, 56–60 (1988).
51. C. C. Ling, M. C. Schell, E. D. Yorke, B. B. Palos and D. O. Kubiawicz and Two-dimensional dose distribution of ^{125}I seeds. *Med. Phys.* **12**, 652–655 (1985).
52. V. Krishnaswamy, Dose distribution around an ^{125}I seed source in tissue. *Radiology* **126**, 489–491 (1978).
53. R. G. Dale, Some theoretical derivations relating to the tissue dosimetry of brachytherapy nuclides, with particular reference to iodine-125. *Med. Phys.* **10**, 176–183 (1983).